Computers in Biology and Medicine 106 (2019) 12–23

Contents lists available at ScienceDirect

Computers in Biology and Medicine

journal homepage: www.elsevier.com/locate/compbiomed

The effects of electrical and thermal boundary condition on the simulation of radiofrequency ablation of liver cancer for tumours located near to the liver boundary

Ean H. Ooi[a,b,*], Khiy W. Lee[a], Shelley Yap[a], Mahmoud A. Khattab[c], Iman Y. Liao[c], Ean T. Ooi[d], Ji J. Foo[a], Shalini R. Nair[e], Ahmad F. Mohd Ali[f]

[a] School of Engineering, Monash University Malaysia, Jalan Lagoon Selatan, 47500, Bandar Sunway, Selangor, Malaysia
[b] Advanced Engineering Platform, Monash University Malaysia, Jalan Lagoon Selatan, 47500, Bandar Sunway, Selangor, Malaysia
[c] School of Computer Science, University of Nottingham Malaysia Campus, Jalan Broga, 43500, Semenyih, Selangor, Malaysia
[d] School of Engineering and Information Technology, Faculty of Science and Technology, Federation University, VIC, 3350, Australia
[e] Department of Radiology, National Cancer Institute, Jalan P7, Presint 7, 62250, Putrajaya, Malaysia
[f] Faculty of Medicine and Health Sciences, University Malaysia Sarawak, 94300, Kota Samarahan, Sarawak, Malaysia

ARTICLE INFO

Keywords:
RFA simulation
Patient-specific model
Liver cancer
Hyperthermia
Thermal therapy

ABSTRACT

Effects of different boundary conditions prescribed across the boundaries of radiofrequency ablation (RFA) models of liver cancer are investigated for the case where the tumour is at the liver boundary. Ground and Robin-type conditions (electrical field) and body temperature and thermal insulation (thermal field) conditions are examined. 3D models of the human liver based on publicly-available CT images of the liver are developed. An artificial tumour is placed inside the liver at the boundary. Simulations are carried out using the finite element method. The numerical results indicated that different electrical and thermal boundary conditions led to different predictions of the electrical potential, temperature and thermal coagulation distributions. Ground and body temperature conditions presented an unnatural physical conditions around the ablation site, which results in more intense Joule heating and excessive heat loss from the tissue. This led to thermal damage volumes that are smaller than the cases when the Robin type or the thermal insulation conditions are prescribed. The present study suggests that RFA simulations in the future must take into consideration the choice of the type of electrical and thermal boundary conditions to be prescribed in the case where the tumour is located near to the liver boundary.

1. Introduction

Radiofrequency ablation (RFA) is a cancer treatment technique that utilizes heat to destroy cancer tissues by way of hyperthermia. Unlike irreversible electroporation, which utilizes very high electrical potential that are delivered at ultra-short pulses, RFA employs low electrical potential that are delivered over an extended period. As such, thermal effects of the former are usually negligible, while the thermal effect from the latter is the primary mechanism of cancer tissue destruction.

Traditionally, computational studies of RFA are carried out by assuming the tissue to have a simplified geometry such as a cylinder or a sphere, which are modelled either in 3D or in 2D axisymmetry coordinates. This approach assumes that the ablation zone is significantly smaller than the actual size of the liver, and that the ablation zone is located sufficiently far away from the liver boundaries such that any boundary effects are negated. The electrical and thermal boundary conditions prescribed across the outer boundaries of these geometrically-simplified models are often ground and body temperature, respectively [1–3]. The former mimics the grounding pad that is placed at the back of patient's thigh, while the latter assumes that normo-thermoregulation of the healthy liver surrounding the modelling domain is sufficient to keep the temperatures at the outer boundaries at body temperature. Some researchers have adopted different types of electrical and thermal boundary conditions, such as the Robin type electrical boundary condition to mimic the outflow of electrical current to an infinite space, and a thermal insulation condition to allow the temperature at the outer boundary to increase in respond to the heating induced by RFA [4–7].

Recently, patient-specific modelling has been gaining attention among doctors, interventional radiologists and biomedical engineers, as

* Corresponding author. School of Engineering, Monash University Malaysia, Jalan Lagoon Selatan, 47500, Bandar Sunway, Selangor, Malaysia.
E-mail address: ooi.ean.hin@monash.edu (E.H. Ooi).

https://doi.org/10.1016/j.compbiomed.2019.01.003
Received 4 December 2018; Received in revised form 4 January 2019; Accepted 5 January 2019
0010-4825/

healthcare gears towards customized and personalized treatments. Patient-specific modelling can be defined as the development of computational models of human pathophysiology that are individualized to patient-specific data [8]. In the treatment of RFA, patient-specific modelling has led to the development of geometrically-accurate models of the liver that are constructed based on images of CT scan that are obtained from actual patients [9–14]. These individualized models are then used by interventional radiologists to predict the outcome of an RFA protocol that is designed specifically for the patient from which the anatomical model was developed.

The use of geometrically-accurate models of the liver to simulate RFA poses two challenges that can affect the accuracy of the numerical results. Firstly, geometrically-accurate models are larger than models with simplified geometry. This translates to a larger mesh density, which require more computational resources in order to solve the model. This becomes problematic if the required computational resources are not available, such that the simulations cannot be completed within a reasonable time. Some researchers have attempted to overcome this by adopting highly efficient numerical techniques such as the Lattice Boltzmann method [11,12], while others have tapped into the resources of graphical processors to speed up the computation [10,13,14]. Payne et al. [13] proposed to resolve this issue by truncating the geometrically-accurate liver model around the tumour region, with the assumption that regions that are far away from the tumour are not affected by the ablation process. Secondly, and more importantly, the use of geometrically-accurate models raises the questions on the appropriate electrical and thermal boundary conditions that are to be prescribed across the outer surfaces of the liver. This is of particular significance in the case where the tumour is located very near to the boundary of the liver.

A tumour that is located very near to the boundary of the liver implies that the ablation site is also located near to the boundary. As such, the typical ground and body temperature conditions, as normally employed when modelling RFA using geometrically-simplified models, may no longer be applicable. Adopting these boundary conditions may subject the model to unnatural electrical and thermal conditions that may give rise to inaccurate predictions of the electro-thermophysiological responses of the tissue during RFA. This may lead to either an overestimation or an underestimation of the induced thermal coagulation, which may lead to fatal consequences if the predictions are translated into actual treatment protocols. An overestimation of the thermal coagulation zone could lead to an incomplete ablation during the actual treatment, while an underestimation could result in over-ablation, where healthy tissues surrounding the tumour are destroyed.

Motivated by this, the present study sets out to investigate the effects of the different electrical and thermal boundary conditions prescribed across the outer boundaries of RFA models for the case where the tumour is located near the liver boundary. For this purpose, the RFA models will be developed based on geometrically-accurate models of the liver. Various cases that are represented by the different combination of electrical (ground and Robin type conditions) and thermal (body temperature and thermal insulation) boundary conditions are examined. The geometrically-accurate models of the liver are constructed using publicly-available CT scan dataset of the liver. An artificial tumour domain represented by an ellipsoid is inserted into the liver in such a way that the tumour domain is positioned at the periphery of the liver. The choice of using an ellipsoid to represent the tumour is arbitrary and one could use a sphere or a cylinder in place of the ellipsoid. In order to reduce the demand for high computational resources, the geometrically-accurate model is truncated around the tumour region, following the suggestion of Payne et al. [13]. Simulations are carried out using the commercial finite element software COMSOL Multiphysics. Investigations are carried out by comparing the volume of the induced thermal damage and the distributions of the temperature, electrical potential and thermal damage for the different cases considered.

2. Methods

2.1. Model geometry

The CT images of the liver are obtained from 3D-IRCADb (3D Image Reconstruction for Comparison of Algorithm Database) [15], a publicly-available database that includes several sets of anonymized medical images of patients and manual segmentation of the various structures of interest performed by clinical experts. The dataset is created by the Institut de Recherche contre les Cancers de l'Appareil Digestif (IRCAD) and is free to be used within the framework of anatomical education or medical simulation [15]. The 3D medical images and masks of the segmented structures of interest are available as DICOM files. Images from 20 patients (10 male and 10 female) are available; of the 20, images from 15 contain the tumour. In the present study, images from two patients; a female patient code named 3D-IRCADb-01 and a male patient code named 3D-IRCADb-05 are used to construct two separate liver models. The 3D liver mesh is reconstructed directly from manually segmented masks that are associated with patients 3D-IRCADb-01 and 3D-IRCADb-05 using the Matlab function ('isosurface.m') with 0.3 isovalue. As the size of the mesh is very large (221,402 vertices and 442,788 faces), a reduction in the resolution that is 0.09% of the original size is carried out using the Matlab function ('reducepatch.m'), resulting in 19,927 vertices and 39,850 faces. Laplacian smoothing is then carried out using the 'smoothpatch.m' function [16]. In the present study, only the liver is segmented, while the presence of the tumour within the CT images is neglected. Instead, the tumour domain is constructed manually based on the shape of an ellipsoid. The choice of using a hypothetical tumour domain is further discussed in Section 4.

Once the smoothed mesh data are obtained, they are imported into the commercial finite element software COMSOL Multiphysics ®, where the geometry of each liver model is constructed. Fig. 1a illustrates the geometry of the liver of patient 3D-IRCADb-01 in the workspace of COMSOL. To construct the tumour domain for patient 3D-IRCADb-01, an ellipsoid of semi-axes 1.25, 1.5 and 1.0 cm in the x-, y- and z-directions, respectively is generated with its centre at $(x, y, z) = (2.6, 1.5, 1)$ cm. This is shown in Fig. 1b, where one may observe that part of the ellipsoid is external to the liver domain. This external domain is deleted and the remaining part of the ellipsoid that is within the liver is assumed to be the tumour (see Fig. 1c). As stated in Section 1, a geometrically-truncated model will be adopted for all simulations in order to reduce the demand for computational resources. To truncate the model, a sphere of radius 6 cm is constructed with its centre placed at the same position as the ellipsoid (see Fig. 1d). The domain that is intersected by the sphere and the liver is taken as the model domain for patient 3D-IRCADb-01 (see Fig. 1e). The model domain for patient 3D-IRCADb-05 is constructed in a similar manner. For this patient, an ellipsoid of semi-axes $(x, y, z) = (1.75, 3, 2)$ cm with its centre placed at (10, 17.5, 4.5) cm is used to construct the tumour domain. Domain truncation is carried out using a sphere of radius 6.5 cm. The construction of the model geometry for patient 3D-IRCADb-05 is shown in the Supplementary Information. Preliminary investigations comparing the simulation results obtained using a geometrically-accurate model and its truncated counterpart did not reveal significant difference between the two; suggesting that the geometrically-accurate model can be replicated at a significantly reduced computational cost using the truncated model.

RFA is carried out by inserting a 17G (radius 0.74 mm) internally-cooled RF probe into the tumour. For patient 3D-IRCADb-01, the RF probe has an active length of 11 mm (including the 1 mm tip) and is inserted along the $y-$axis. For patient 3D-IRCADb-05, the RF probe has an active length of 21 mm (including 1 mm tip) and is inserted vertically from the z-axis. The difference in the active length for the different patients is to account for the different tumour sizes constructed using the different ellipsoid sizes. In order to simplify the notation used in the present paper, the models developed using data from patients 3D-

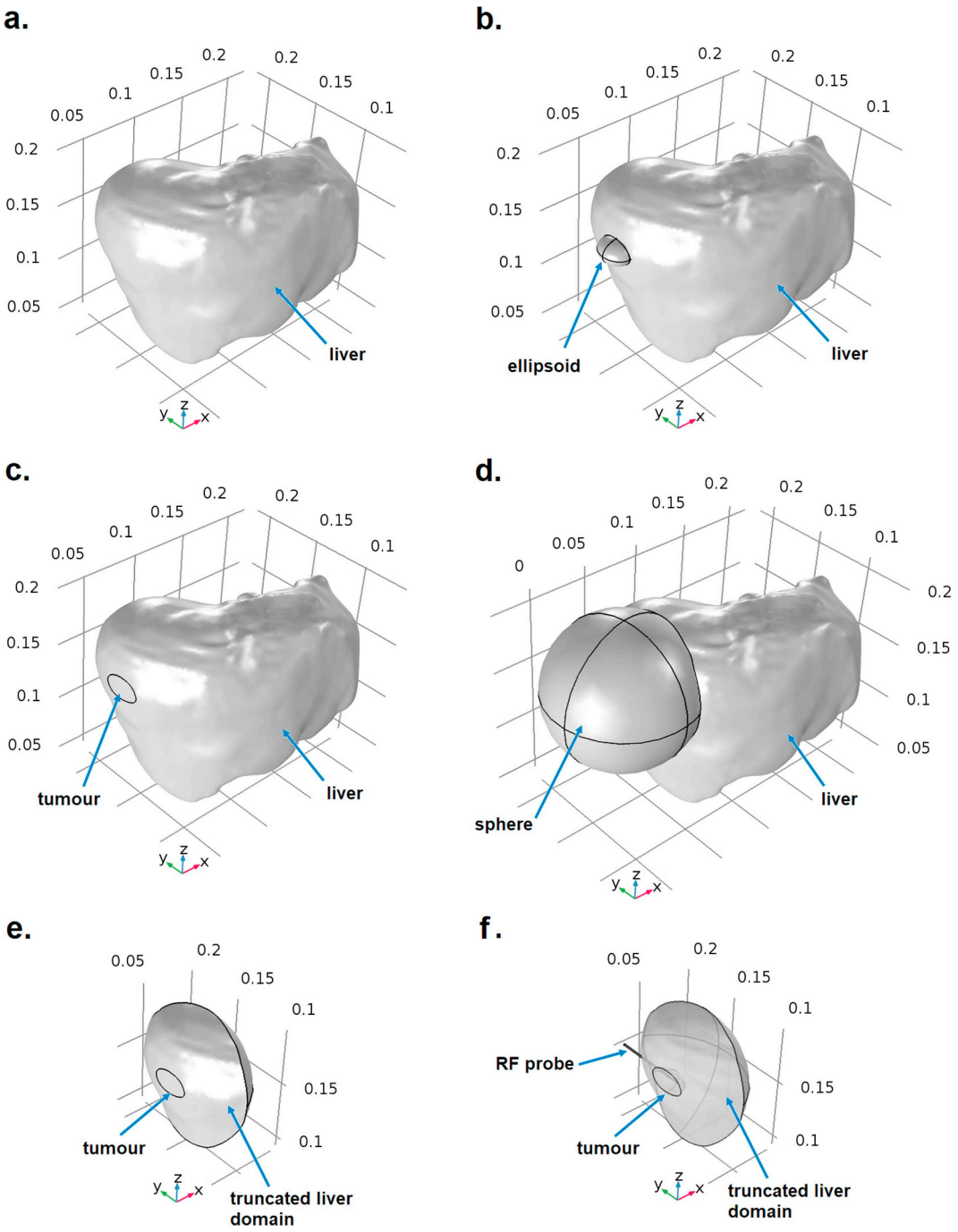

Fig. 1. a. The liver model obtained after segmentation of the CT images, b) construction of an ellipsoid, c) removal of part of the ellipsoid domain exterior to the liver, d) construction of the sphere to truncate the liver model, e) the resulting truncated liver model, f) the RF probe in place inside the tumour. Figures are representative that of Model A.

IRCADb-01 and 3D-IRCADb-05 are hereafter referred to as Model A and Model B, respectively.

2.2. Governing equations

For the range of frequency used in the treatment of RFA (400–500 kHz), the electrical potential distribution inside the tissue can be expressed by using the quasistatic approximation of the Maxwell equation [17]:

$$\nabla\cdot(\sigma(T)\nabla\phi) = 0, \tag{1}$$

where $\sigma(T)$ is the temperature-dependent tissue electrical conductivity and ϕ is the electrical potential distribution.

The transient temperature distribution inside the tissue during RFA is described using the Pennes bioheat equation [18]:

$$(\rho c)_{eff}\frac{\partial T}{\partial t} = \nabla\cdot(k(T)\nabla T) + \rho_b c_b \omega_b (T_b - T) + q_h, \tag{2}$$

where T is tissue temperature, T_b is blood temperature, t is time, $k(T)$ is the temperature-dependent thermal conductivity, c_b is the specific heat of blood, ω_b is the blood perfusion rate and q_h is the amount of heat deposited into the tissue due to Joule heating, which is obtained from:

$$q_h = \sigma(T)|\nabla\phi|^2. \tag{3}$$

The bioheat equation shown in Eq (2) must be able to account for the thermal effects due to phase change. Phase change occurs when water inside the tissue vaporizes as the tissue temperature elevates beyond the vaporization threshold. In order to account for the phase change effects, the apparent heat capacity method is used [17], which expresses the term $(\rho c)_{eff}$ in Eq (2) as:

$$(\rho c)_{eff} = \begin{cases} \rho c, & T \le T_l \\ \frac{\rho c + (\rho c)_{vap}}{2} + \frac{\rho_w h_{fg} \beta}{T_u - T_l}, & T_l < T \le T_u \\ (\rho c)_{vap}, & T > T_u, \end{cases} \tag{4}$$

where the subscripts '*vap*' and '*w*' represent vapour and water, respectively, h_{fg} is the latent heat of vapourisation, $T_l = 99°C$ and $T_u = 100°C$ are the lower and upper temperatures of phase change, respectively and β is the tissue water content.

The thermal damage sustained by the tissue during RFA is quantified using the Arrhenius thermal damage model [19], which is given by:

$$\Omega(\mathbf{r}, t) = \int_0^{t_f} A \exp\left(-\frac{\Delta E}{RT(\mathbf{r}, t)}\right) dt, \tag{5}$$

where Ω is a parameter that quantifies the amount of thermal damage inside the tissue, t_f is the time at which the thermal damage is evaluated, A is the frequency factor, ΔE is the activation energy that represents irreversible thermal energy damage reaction and R is the universal gas constant.

2.3. Boundary conditions

Across the active part of the probe, a time-dependent electrical potential is prescribed, such that:

$$\phi(t) = \phi_{app}(t), \tag{6}$$

where $\phi_{app}(t)$ is the applied voltage and has an initial value of 70 V. The transient variation in $\phi_{app}(t)$ is governed by the impedance-controlled algorithm, which is further explained in Section 2.5.5. Since an internally-cooled RF probe is used to carry out the ablation, the thermal boundary condition across the active part of the probe can be written as [20]:

$$-k\frac{\partial T}{\partial n} = h_{cool}(T - T_{cool}), \tag{7}$$

where h_{cool} is the convection heat transfer coefficient and T_{cool} is the temperature of the internally-circulating liquid. Eq (7) describes the convective heat transfer between the internally-circulating liquid and the surrounding tissue. In the present study, the flow rate of the internally-circulating liquid is chosen to be 100 ml/min. This results in a value of h_{cool} of 5646 W/m^{2}K that is calculated based on the estimation approach of Burdío et al. [20]. The temperature of the internally-circulating liquid is chosen to be 2 °C. The selected flow rate and temperature combination is sufficient to maintain the temperature along the surface of the probe to around 20 °C during RFA.

The type of electrical and thermal boundary conditions applied to the exterior boundaries of the model vary. As discussed in Section 1, two of the most common boundary conditions used in RFA simulations are the ground and the Robin type conditions for the electric field, and body temperature and thermal insulation for the temperature field. Ground condition is represented by a zero electrical potential, i.e.:

$$\phi = 0\ \text{V}, \tag{8}$$

while the Robin type boundary condition is expressed mathematically as [4,6,21]:

$$\frac{\partial \phi}{\partial n} = -\frac{\mathbf{n}\cdot(\mathbf{r} - \mathbf{r_o})}{|\mathbf{r} - \mathbf{r_o}|^2}\phi, \tag{9}$$

where $\mathbf{n}$ is the unit normal vector, $\mathbf{r}$ is the position vector in space and $\mathbf{r}_o$ is the position vector of a point at the centre of the active part of the RF probe. The body temperature condition is given by:

$$T = 37°C, \tag{10}$$

while the thermal insulation condition is expressed as:

$$-k\frac{\partial T}{\partial n} = 0. \tag{11}$$

Four cases are considered in the present study. In Case 1, ground and body temperature conditions are prescribed across the exterior boundaries of the model. In Case 2, ground and thermal insulation conditions are prescribed across the exterior boundaries. Case 3 prescribes the Robin type and body temperature conditions across the exterior boundaries, while Case 4 prescribes the Robin type and thermal insulation conditions across the exterior boundaries.

2.4. Initial condition

The initial temperature of the model is set to 37 °C, which represents the body temperature. For the thermal damage model, an initial condition of Ω= 0 is assigned, since no thermal damage occurs inside the tissue prior to ablation.

2.5. Material properties

Except for the tissue electrical conductivity, thermal conductivity and blood perfusion rate, all the electrical, thermal and physiological parameters of the tissue pertaining to the model are assumed to be constants. Their values are summarized in Table 1 along with the sources from where they are obtained.

2.5.1. Temperature-dependent electrical conductivity

Various temperature-dependent electrical conductivity models have been reported in the literature [17,22,23], with the variation likely to be caused by the different methods of measurement and the use of different types of biological tissues as test samples. The model proposed by Trujillo et al. [2] is used in the present study, which is given by:

$$\sigma(T) = \begin{cases} \sigma_o \exp(0.015(T - T_{ref})), & T \le T_l \\ 2.5345\sigma_o, & T_l < T \le T_u \\ 2.5345\sigma_o - 0.50183\sigma_o(T - T_u), & T_u < T \le T_u + 5 \\ 0.025345\sigma_o, & T > T_u + 5 \end{cases}, \tag{12}$$

where σ_o is the electrical conductivity of the liver (or the tumour) at baseline temperature T_{ref}, and T_l and T_u are the lower and upper phase change temperatures, respectively. Eq (12) describes an exponential increase of σ with temperature up until the tissue temperature approaches the threshold for water vaporization; after which the tissue electrical conductivity drops by two orders of magnitude. It is important to note that the other temperature-dependent electrical conductivity models that are available in the literature (see the review by Trujillo and Berjano [22]) also describe a similar behaviour, albeit with some slight variations. Nevertheless, these slight variations have been shown to have no significant effect on the calculation of lesion diameter following RFA [22].

2.5.2. Temperature-dependent thermal conductivity

The thermal conductivity of the liver and the tumour are assumed to increase linearly with temperature following the function Hall et al. [23]:

$$k(T) = \begin{cases} k_o + \Delta k(T - T_{ref}), & T \le T_u \\ k_o + \Delta k(T_u - T_{ref}), & T > T_u \end{cases}, \tag{13}$$

where k_o is the thermal conductivity of the liver (or the tumour) measured at baseline temperature T_{ref} and Δk is the increase of the liver (or the tumour) thermal conductivity per degree Celcius increase in temperature.

Table 1
Values of the material properties used in the present study.

Parameter	Value	References
Electrical model		
Baseline liver electrical conductivity, σ_0 (S/m)	0.33	[31]
Baseline tumour electrical conductivity, σ_0 (S/m)	0.45	[32]
Vapour electrical conductivity, σ_{vap} (S/m)	$0.001\sigma_0$	[31]
Probe electrical conductivity, σ_{probe} (S/m)	10^8	[31]
Shaft electrical conductivity, σ_{shaft} (S/m)	4×10^6	[31]
Thermal model		
Liver thermal conductivity, κ_{liver} (W/m·K)	0.512	[31]
Tumour thermal conductivity, κ_{tumour} (W/m·K)	0.511	[33]
Liver & tumour density, ρ (kg/m^3)	1060	[31]
Liver & tumour heat capacity, C (J/kg·K)	3600	[31]
Probe thermal conductivity, κ_{probe} (W/m·K)	18	[31]
Probe density, ρ_{probe} (kg/m^3)	6450	[31]
Probe heat capacity, C_{probe} (J/kg·K)	840	[31]
Shaft thermal conductivity, κ_{shaft} (W/m·K)	71	[31]
Shaft density, ρ_{shaft} (kg/m^3)	21,500	[31]
Shaft heat capacity, C_{shaft} (J/kg·K)	132	[31]
Blood density, ρ_b (kg/m^3)	1000	[31]
Blood heat capacity, Cb (J/kg·K)	4180	[31]
Baseline liver blood perfusion rate, ω_b (1/s)	0.0064	[31]
Baseline tumour blood perfusion rate, ω_b (1/s)	0.0042	[34]
Latent heat of vapourisation, h_{fg} (J/kg)	2.26×10^6	Assumed as water
Tissue water content, β	0.71	[23]
Heat capacity of water vapour, $(\rho c)_{vap}$ (J/m^3·K)	6×10^5	[23]
Thermal damage model		
Liver		
Frequency factor, A (1/s)	7.39×10^{39}	[35]
Activation energy, ΔE (J/mol)	2.5775×10^5	[35]
Tumour		
Frequency factor, A (1/s)	3.247×10^{43}	[36]
Activation energy, ΔE (J/mol)	2.814×10^5	[36]

2.5.3. Thermal coagulation volume

As shown in Eq (5), Ω determines the amount of thermal coagulation sustained by the tissue during RFA. According to Trujillo et al. [2], a value of Ω= 4.6 is a good indicator for complete thermal coagulation of the tissue. Hence, to determine the volume of thermal coagulation induced by RFA, a volumetric integral of the model across the nodes with Ω≥ 4.6 is performed.

2.5.4. Damage-dependent blood perfusion rate

Blood perfusion through the micro capillaries inside the tissue acts as a heat sink that draws heat away from the tissue during RFA. As the tissue temperature increases beyond the thermal damage threshold, the micro capillaries eventually rupture such that blood flow ceases to exist. In the present study, complete cessation of blood perfusion is assumed to occur at the onset of complete thermal coagulation, i.e. at the threshold of Ω= 4.6. As such, the parameter ω in Eq (2) can be expressed as a function of Ω, such that:

$$\omega(\Omega) = \begin{cases} \omega_b, \Omega \leq 4.6 \\ 0, \ \Omega > 4.6 \end{cases}, \tag{14}$$

where ω_b is the baseline blood perfusion rate of the liver (or the tumour).

2.5.5. Impedance-controlled ablation

The RFA protocol implemented in the present study follows closely the optimized impedance-controlled ablation protocol proposed by Goldberg et al. [24], which was introduced as a way to prevent the stoppage of ablation when complete water vaporization of the tissue surrounding the RF probe occurs. In this protocol, ablation is carried out by applying a constant electrical potential across the active part of the electrode (see Eq (6)) until the tissue impedance increases to 30 Ω above its initial value. At this point, ablation is stopped by setting $\phi_{app}(t) = 0$ V for 20 s, after which the ablation process is restarted. An optimized ablation protocol, also proposed by Goldberg et al. [24], that reduces the input electrical potential by 5 V when the ablation duration from the previous heating cycle is less than 10 s is also implemented in the present model to maximize the ablation process. The implementation of the impedance-controlled algorithm requires the knowledge of the tissue impedance during RFA, which can be calculated using [23]:

$$Z(t) = \iiint_V \frac{\phi_{app}^2(t)}{Q_{tot}} dV, \tag{15}$$

where V is the volume of the tissue and Q_{tot} is the total RF energy absorbed by the tissue.

2.6. Mesh convergence

A mesh convergence study is carried out to determine the optimal number of elements that would result in numerical solutions that are independent of the mesh size. The model is discretized into tetrahedral elements, with first order approximations applied to all the physical variables considered. The tumour domain is given extra refinements compared to the liver domain, since the majority of the physical variables variation are expected to occur here. Very fine triangular elements are also prescribed across the surface of the RF probe. Mesh convergence study is carried out by systematically decreasing the maximum element size from 8 to 2 mm for the tumour domain and from 10 to 3 mm for the tissue domain. Convergence is checked for the temperature that is measured at nine points located around the RF probe and the thermal coagulation volume. These points were chosen to be near to the RF probe so that the convergence can be monitored for points that are sensitive to the changes in the physical variables, i.e. the electrical potential, temperature and thermal coagulation.

Fig. 2b shows the percentage difference in the temperature across the nine sampling points and the thermal coagulation volume obtained for Model A for the different mesh setting when the maximum element sizes for the tumour and the liver are decreased. Data for Model B are available in the Supplementary Information. Decreasing the maximum element sizes led to very little change in the coagulation zone volume (less than 3.2%), while data for temperature showed less than 3% variation in their values. For Model B, the percentage difference as the maximum element size is decreased is less than 1% for both the coagulation zone volume and the average temperature across the 9 sampling points. Based on the mesh convergence study, maximum element sizes of 3 and 5 mm are chosen for the tumour and tissue domains, respectively for Model A; while 2 and 4 mm were chosen for Model B. This resulted in 101,109 tetrahedral elements for Model A and 133,626 for Model B. Fig. 2c illustrates Model A in its discretized form, while Fig. 2d shows a view of the interior mesh structure along with an enlarged view of the fine surface discretization across the RF probe.

2.7. Model verification

In order to verify the accuracy of the numerical model developed in this study, the parameters and the settings of the RFA model are adjusted to mimic as close as possible the *ex vivo* experimental study reported by Goldberg et al. [24]. For this purpose, a spherical tissue model in the 2D axisymmetry coordinates is developed. Blood perfusion is set to zero to replicate the absence of blood flow inside *ex vivo* tissues. The internally-cooled RF probe has an active length of 3 cm and a diameter of 1.3 mm, corresponding to an 18G needle. Temperature of the internally-circulating coolant is 0 °C. Goldberg et al. [24] reported a coolant flow rate of 10–25 ml/min. In the present study, a flow rate of 25 ml/min is chosen. The initial electrical potential applied to the surface of the RF probe is set to 85 V after several trial and error

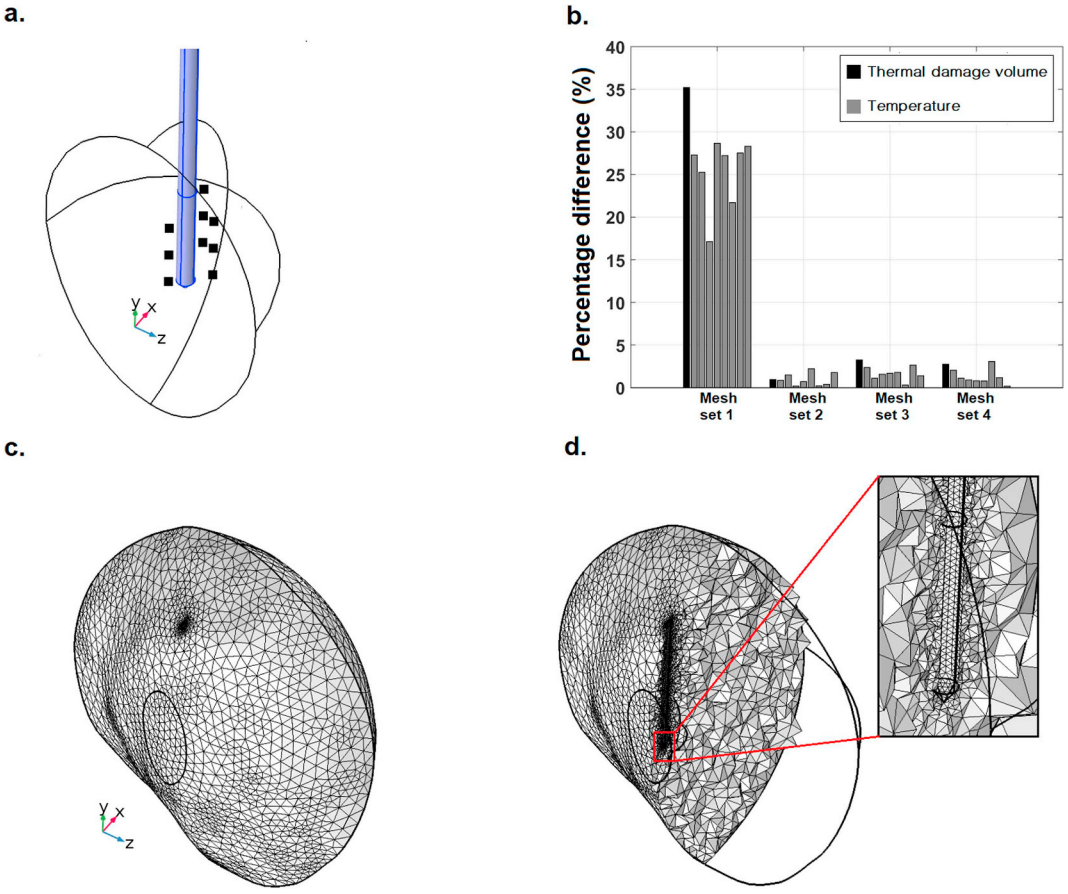

Fig. 2. a) The nine sampling points chosen near the RF probe, b) results from the mesh convergence test, where the data for temperatures are collected across nine sampling points, c) the truncated model domain discretized into tetrahedral elements, d) cut-view of the tetrahedral elements and the surface discretization of the RF probe.

simulations to match the total current delivery and the tissue impedance profiles between the model and the experimental results.

Fig. 3 compares the tissue impedance profiles between the present model and the study of Goldberg et al. [24]. Good agreement between the two is observed. The model predicted 25 pulses, while the experimental study found 27 pulses. The initial tissue impedance was predicted to be approximately 85.7 Ω, which is lower than the value found experimentally (100 Ω). The first roll-off of the model occurs at 42 s, while a value of 55 s is estimated from the experiments. The discrepancies may be due to the variation in the material properties

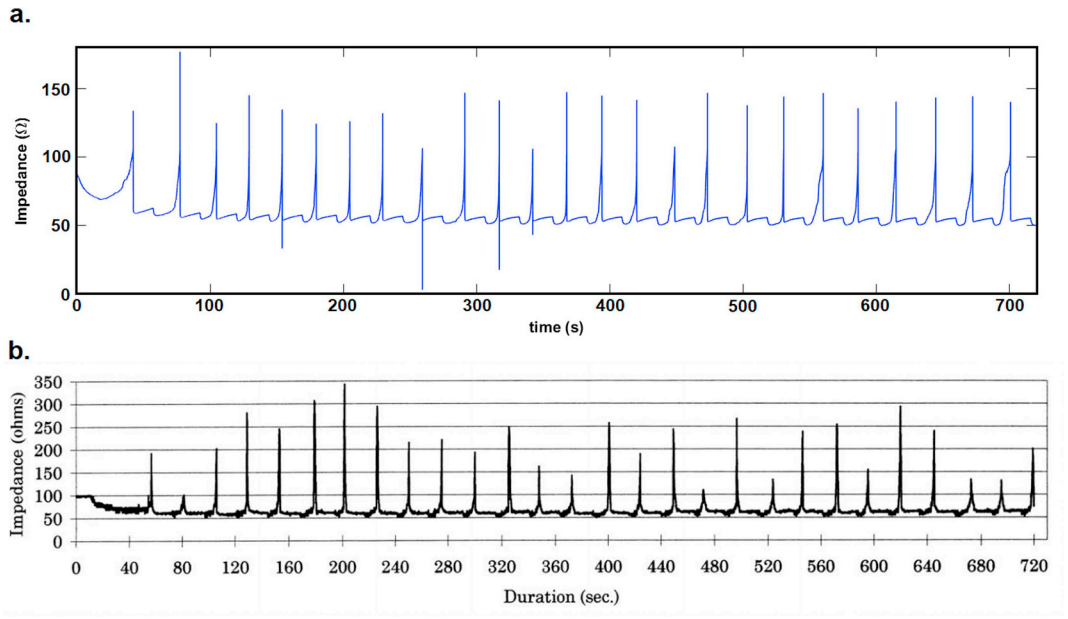

Fig. 3. Comparison of the tissue impedance plot between a) the numerical model and b) the experimental results of Goldberg et al. [24].

Table 2
Comparison of the thermal coagulation volume and maximum tissue temperature measured between the numerical model and the experimental study of Goldberg et al. [24].

	Present model	Goldberg et al. [24]
Thermal coagulation diameter (cm)	3.64	4.6 ± 0.2
Maximum temperature (°C)		
5 mm	97.38	100.4 ± 1.4
10 mm	77.07	79.5 ± 4.7
15 mm	59.25	57.3 ± 4.2
20 mm	46.00	46.2 ± 4.4

between the actual liver in the experiments and the value used in the numerical model and some modelling parameters, such as the flow rate of the coolant, which were presented as a range rather than a single value. It is noteworthy that the discrepancies between the numerical and experimental results are prominent only during the initial stages of ablation. This argument can be supported by observing the time for the optimized algorithm to first take effect, i.e. the first instance the applied voltage is reduced by 5 V (see Section 2.5.5). It is found that only 1 s separated the first occurrence of roll-off (144 vs 145 s) between the numerical model and the experiment.

Table 2 compares the thermal coagulation diameter and the maximum tissue temperature measured at 5, 10, 15 and 20 mm from the RF probe between the present model and the results by Goldberg et al. [24]. The model predicted a thermal coagulation diameter of 3.64 cm, which is approximately 21% smaller than the value obtained experimentally (4.6 ± 0.2 cm). The difference may be due to the experimental value being assessed based solely on visualization of the coagulation zone. Good agreement in the maximum tissue temperatures at the four points was obtained, however.

The good agreement between the numerical results and the experimental findings as presented in Fig. 3 and Table 2 suggests that the numerical model developed in the present study can replicate the outcomes of an actual RFA treatment within reasonable accuracy.

3. Results

The effects of the different boundary conditions identified by the different cases in Section 2.3 are investigated for an ablation protocol of 600 s. The optimized impedance-controlled algorithm discussed in Section 2.5.5 is effective throughout the 600 s of ablation time. The models are solved using COMSOL Multiphysics 5.3 based on a segregated solver and an adaptive time-stepping scheme. The time steps employed by the solver ranged from approximately 0.0018 to 7 s. The shorter time steps are generally used during the heating phase, while the longer time steps are used during the cooling phase. In what follows, only the results obtained for Model A are presented. The results obtained using Model B, which share similar observations as that of Model A are available in the Supplementary Information.

In order to understand how the different boundary conditions affect the temporal ablation process, the tissue impedance is plotted against time for each of the four cases investigated. This is shown in Fig. 4. Each peak in the graph represents the period when the RF system is active. Cases 1 and 2 showed very similar impedance profiles, with an initial impedance of approximately 60 Ω and a total of 20 peaks. On the other hand, Cases 3 and 4 have similar impedance profiles, with an initial impedance of approximately 130 Ω and a total of 19 heating peaks obtained. For Cases 1 and 2, the first roll-off occurs at approximately 2.5 s. This is indicated by the red arrow in the inset of Fig. 4a. Roll-off is defined as the sudden increase in tissue impedance as a result of water vaporization inside the part of tissue surrounding the RF probe such that RF energy delivery is impeded [25]. For Cases 3 and 4, the first roll-off occurs at approximately 12 s after the start of ablation. These findings indicate that there are variations to the temporal ablation

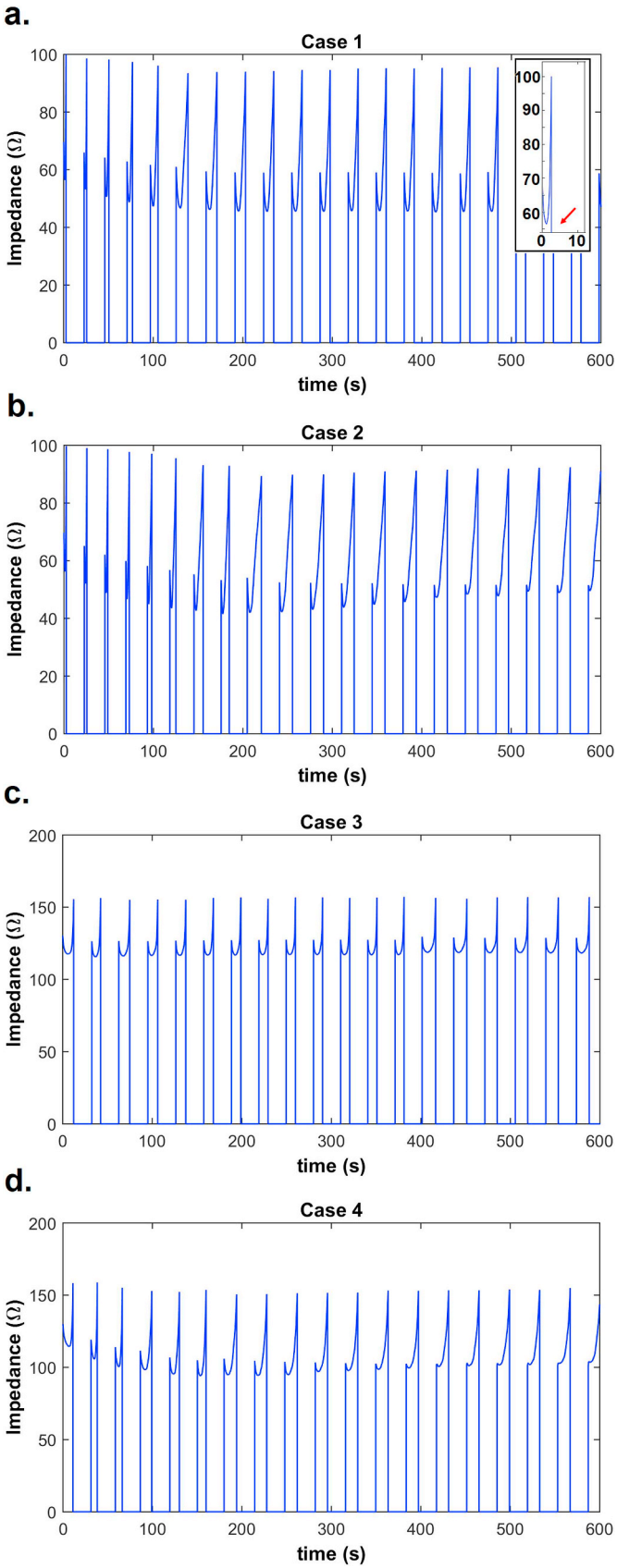

Fig. 4. Plots of the temporal variation in the tissue impedance for Model A obtained for a) Case 1 (inset shows an enlarged section indicating the onset of the first roll-off), b) Case 2, c) Case 3, and d) Case 4.

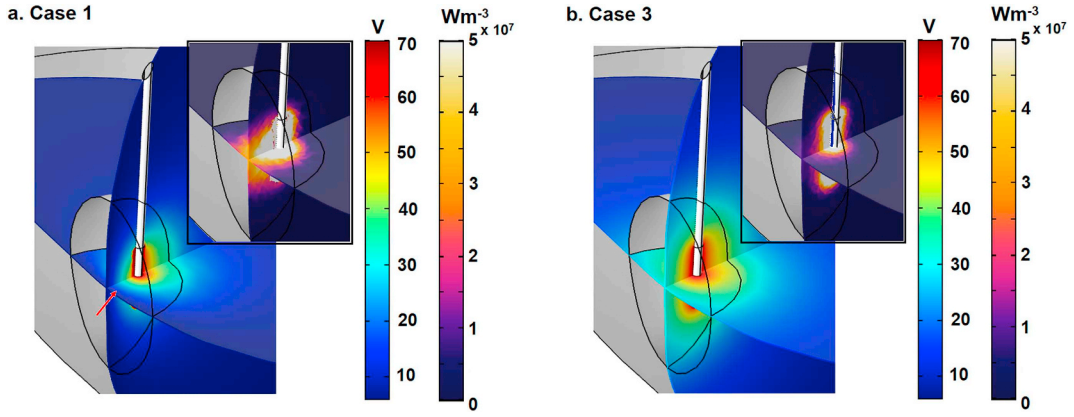

Fig. 5. Contours of the electrical potential distribution and Joule heating (inset) obtained for a) Case 1 and b) Case 3 of Model A.

profiles when different electrical and thermal conditions are prescribed across the exterior boundaries of the model. Nevertheless, the similarity in the impedance profiles between Cases 1 and 2; and between Cases 3 and 4 suggests that the electrical boundary condition plays a more dominant role than the thermal boundary condition.

In order to understand the cause for the rapid occurrence of roll-off observed for Cases 1 and 2, the electrical potential distribution across the $y = 15$ cm and $z = 15$ cm planes at $t = 2$ s, i.e. the time step just before the first occurrence of roll-off, obtained for Case 1 are plotted. This is shown in Fig. 5a. The proximity of the RF probe to the model boundary and the prescription of ground condition to the exterior boundaries results in a large spatial variation of the electrical potential in the region surrounding the probe (see red arrow). This gives rise to a large electrical potential gradient, $\nabla\phi$, which results in a more intense and widespread Joule heating in the region surrounding the RF probe (see Fig. 5a inset), following Eq. (3). The intense Joule heating results in a rapid temperature rise to levels that cause complete vaporization of water inside the tissue, which hastened the first roll-off process. Conversely, for Cases 3 and 4, the Robin-type boundary condition allows the natural flow of electrical current away from the centre of the active probe. Consequently, there is a more homogeneous distribution of electrical potential distribution across the tissue, such as shown in Fig. 5b for Case 3 at $t = 2$ s. The smaller spatial variation in the electrical potential distribution meant that Joule heating is weaker (see Fig. 5b inset), which delays the onset of the first roll-off.

Fig. 6 plots the contours of the temperature distribution across the $y = 15$ cm and $z = 15$ cm planes for Cases 1 to 4. Different time levels were chosen for each case since the type of boundary conditions prescribed affected the temporal ablation process of the tissue (see Fig. 4). The time levels were chosen such that they complete one heating-cooling cycle. With Case 1, the body temperature condition prescribed across the exterior boundaries of the model restricted the spread of temperature increase in the region between the RF probe and the exterior boundary. This is indicated by the red arrow in Fig. 6a at $t = 300$ s. During the cooling phase ($t = 306$–318 s), the body temperature condition acts as a heat sink that results in a large drop in tissue temperature. This is indicated by the black arrows in Fig. 6a. A similar observation can be made for Case 3 (see Fig. 6d). With Cases 2 and 4, the thermal insulation condition allowed the tissue temperature in the region between the RF probe and the exterior boundary to increase in response to Joule heating. This is shown by the red arrows in Fig. 6b. Nevertheless, during cooling, the implementation of the thermal insulation condition meant that cooling can only occur through the surface of the RF probe (see black arrows in Fig. 6b) and not through the exterior boundaries of the liver. As such, temperature across the majority of the tissue surrounding the probe remains high during the cooling phase ($t = 332$–344 s for Case 2 and $t = 366$–378 s for Case 4).

Fig. 7 plots the contours of the thermal damage after 10 min of RFA for Cases 1 to 4. Thermally-damaged regions are indicated in red, while blue represents region without thermal damage (or unablated tissues). Cases 1 and 3 showed signs of incomplete thermal ablation across the tumour region, particularly in the area next to the exterior boundary where the body temperature condition is prescribed (see red arrows in Fig. 7a and c). This is well-correlated with the regions of low temperature due to the prescription of the body temperature condition, as seen in Fig. 6a and c. In Cases 2 and 4, no signs of incomplete thermal ablation can be found. In fact, one may observe that the region of thermal damage extends beyond the tumour margins, as indicated by the green arrows in Fig. 7b and d. Unlike Cases 1 and 3, the thermal insulation condition allows the temperature at the exterior boundary to increase in response to Joule heating. This causes the temperature to increase to levels that are sufficient for thermal damage to occur.

The volume of thermal damage obtained for Model A for Cases 1 to 4, along with their percentage difference for the different boundary conditions combinations, are tabulated in Table 3. The combination of ground and body temperature conditions (Case 1) produces the smallest volume, while the combination of the Robin type and thermal insulation conditions (Case 4) produces the largest volume. By fixing the electrical boundary condition to ground (Cases 1 and 2), an increase in the thermal damage volume of approximately 70% is observed when the thermal boundary condition changes from body temperature to thermal insulation. When the electrical boundary condition is fixed to the Robin type condition (Cases 3 and 4), the differences in the thermal damage volume is approximately 30%. Now when the thermal boundary condition is fixed to body temperature (Cases 1 and 3), the thermal damage volume obtained for Case 3 is 48% larger than that of Case 1. On the other hand, when thermal insulation condition is fixed (Cases 2 and 4), the difference in the volume is only 13%. These results suggest that the RFA models have a higher sensitivity to the thermal boundary condition than the electrical boundary condition.

4. Discussions

The advancement of patient-specific modelling in the RFA treatment of liver cancer has led to the development of individualized liver models that are constructed based on CT scan images of actual patients. Several studies have explored more effective ways to simulate RFA using these patient-specific models, such as the use of Lattice Boltzmann method [11,12] and the utilization of GPUs for simulations [10,13,14]; however, very little attention has been paid to the proper prescription of boundary conditions, especially when the tumour is located next to the boundary of the liver. The proximity of the tumour to the exterior boundaries of the liver suggests that the type of boundary conditions prescribed could significantly affect the prediction outcomes of RFA models, since the boundaries are no longer sufficiently

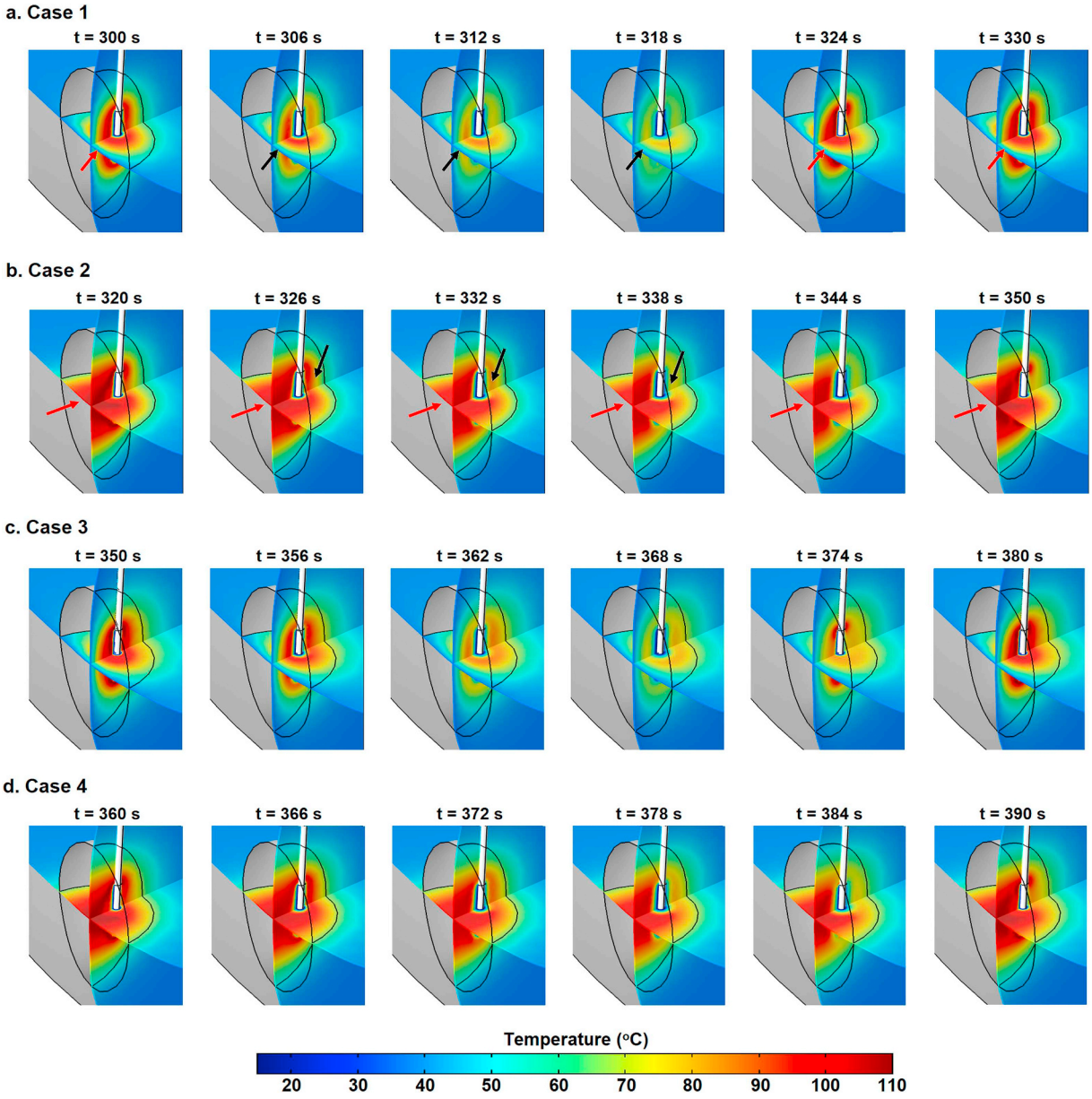

Fig. 6. Contours of the temperature distribution at various time steps for a) Case 1, b) Case 2, c) Case 3, and d) Case 4 of Model A.

far away from the ablation site. This can have important consequences, especially in patient-specific modelling, where the computational models are used to facilitate with the planning of the ablation protocol to be given to a particular patient.

The ground condition mimics the ground pad that is commonly placed at the back of the patient's thigh during RFA. In contrast, the Robin type boundary condition simulates the natural flow of the electrical current from the RF probe to the surrounding open space. For the cases considered in the present study, where the tumour is located near to the exterior boundary, the ground condition imposes an artificially low electrical potential in the vicinity of the RF probe. In reality, the boundaries of the liver would still be at a distance away from the actual ground pad. As such, it is unlikely for the liver to have a zero electrical potential distribution (see Fig. 5a), particularly in the part of the exterior boundary that belongs to the tumour. The ground condition causes a large spatial variation in the electrical potential distribution that results in Joule heating that are so intense that the first onset of roll-off occurs at approximately 2.5 s after the start of ablation. The more intense Joule heating does not translate to more effective ablation, as the majority of the treatment duration are spent on the cooling phase. When the Robin type boundary condition is applied, one may observe that the electrical potential distribution across the exterior liver boundaries is not zero. Instead, values ranging from 30 to 40 V can be observed (see Fig. 5b). If the Robin type boundary condition does indeed replicate more accurately the tissue electrical response, then one may conclude that the ground condition underestimates the magnitude of the electrical potential distribution across the exterior boundary by 30–40 V.

The different thermal boundary conditions were also found to affect the prediction outcome of RFA models. The body temperature condition generally assumes the ablation zone to be sufficiently isolated such that normo-thermoregulation from the surrounding healthy tissues can maintain the temperature at the exterior boundaries of the model domain at body temperature. In the case where the tumour is located next to the exterior liver boundary, the body temperature condition becomes a heat sink that constantly draws heat away from the ablation zone. During the heating phase, this condition prevented the tissue temperature near to the boundary to increase naturally in response to Joule

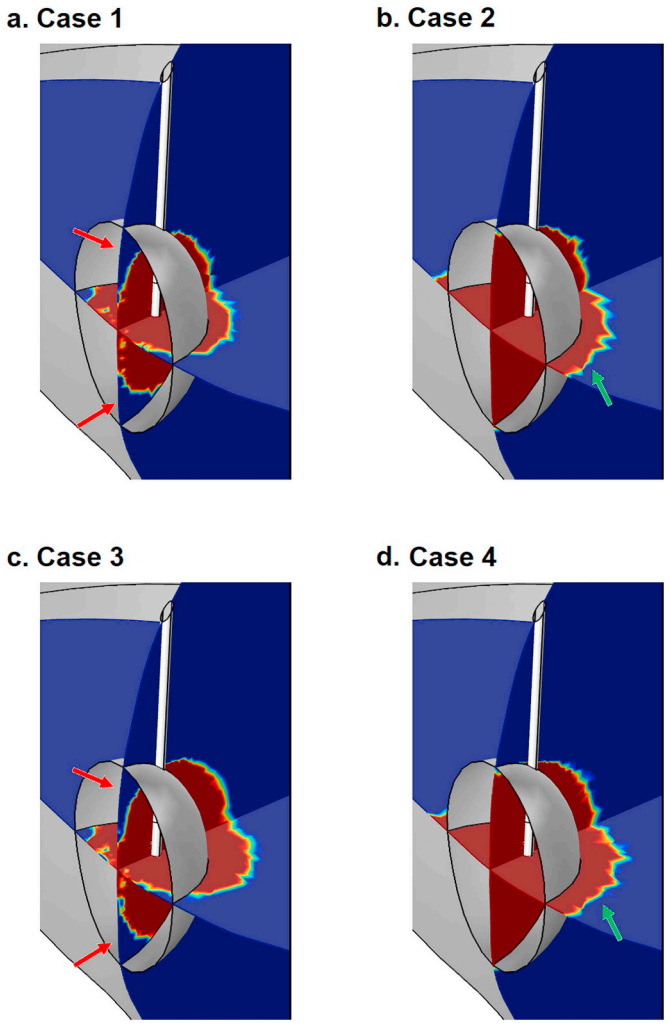

Fig. 7. Contours of the thermal damage obtained after 10 min of RFA for a) Case 1, b) Case 2, c) Case 3, and d) Case 4 of Model A.

Table 3
Volume of thermal damage obtained for Cases 1 to 4 of Model A.

Combination	Volume (cm^3)	Difference
Ground condition		
Body temperature (Case 1)	3.629	69.6%
Thermal insulation (Case 2)	6.154	
Robin-type condition		
Body temperature (Case 3)	5.370	29.7%
Thermal insulation (Case 4)	6.966	
Body temperature		
Ground condition (Case 1)	3.629	48%
Robin-type condition (Case 3)	5.370	
Thermal insulation		
Ground condition (Case 2)	6.154	13.2%
Robin-type condition (Case 4)	6.966	

heating. During the cooling phase, this condition promotes greater heat loss from the tissue, which resulted in less effective ablation during the next ablation cycle, since part of the electromagnetic energy is used to raise the temperature instead of ablating the tissue. Both phenomena contribute to the less effective RFA treatment observed in Cases 1 and 3, as indicated by their smaller thermal coagulation volume compared to Cases 2 and 4, respectively.

The results presented in Section 3 represent that of Model A. Results obtained for Model B, with a different tumour size and orientation, showed similar outcomes (see Supplementary Information). This suggests that the results presented in Section 3 are and the inference on the influence of the electrical and thermal boundary conditions are not specific to Model A. Similar outcomes are expected when the model is constructed using data from different patients and with different tumour shapes and sizes, provided that the tumour is located near to the boundary of the liver. If the tumour is located at a distance away from the liver boundary, the different electrical and thermal boundary conditions are not expected to significantly influence the prediction outcomes. To support this, simulations are repeated for a specific case where the entire tumour is located within the liver and at a distance away from the liver boundary. To do so, an ellipsoid of semi-axes 1.25, 1.5 and 1.0 cm in the x-, y- and z-directions, respectively is constructed and is placed inside the liver of patient 3D-IRCADb-01 with its centre at the coordinates (8, 17, 14) cm. The model is then truncated using a sphere of radius 4.5 cm. Simulations are repeated using this model, hereafter referred to as Model C, and the results are summarized in Fig. 8 for the contours of electrical potential, temperature and thermal coagulation distribution. The volume of thermal coagulation obtained for Cases 1 to 4 of Model C are presented in Table 4. Overall, very little difference in the prediction of electrical potential, temperature and thermal coagulation distributions can be observed across the four cases examined using Model C, which suggests that the electrical and thermal boundary conditions have very minimal influence if the tumour is located sufficiently far from from the liver boundary.

Verification of the developed mathematical model against experimental studies reported in the literature showed good agreement, which lends credence to the accuracy of the RFA model. However, experimental studies to accompany the present computational efforts have not been carried out due to the lack of the necessary resources needed to carry out the intended experiments. As such, it is not possible at this stage to conclude whether the ground or the Robin type boundary condition, and the body temperature or thermal insulation conditions are better at simulating RFA of liver cancer when the tumour is located next to the liver boundary. Nevertheless, analyses of the current results coupled with experimental and clinical observations reported in the literature suggest that the results obtained using the model employing the Robin type condition and the thermal insulation condition are more realistic. This is based on several clinical reports that found extra-hepatic complications as the direct results of thermal injury due to heat conduction from the ablation zone to the neighbouring organs, such as the bowel, the colon and the stomach [26–29]. As shown in Fig. 6a and c, the body temperature condition imposes an artificial boundary heat sink that restricted the tissue temperature rise and thus, the formation of thermal coagulation in the region near to the liver boundary. This condition fails to capture the rise in the exterior boundary temperature as heat conducts from the liver into the nearby organs.

Justification for the Robin type boundary condition can be made by comparing the first roll-off occurrence against the same values that have been reported in experimental studies from the literature. In general, the ground condition causes the first roll-off of the RF system to occur at approximately 2.5 s. To the authors' knowledge, such a rapid first roll-off of the RF system due to water vapour surrounding the RF probe has never been observed. The majority of the studies available in the literature have reported values ranging from 60 to 90 s [24,25,30]. In contrast, the first roll-off occurs at approximately 12 s when the Robin type boundary condition is used. Admittedly, this value is still far from the range of values obtained experimentally and it is possible that this may be due to the tumour being located very near to the boundary of the liver. Examination on Model C revealed that the first roll-off occurs at approximately 40 s when the ground condition is applied and 105 s when the Robin type condition is applied, which are closer to the experimental studies. This finding partially supports the argument that the Robin type boundary condition is better suited for RFA simulations than the ground condition. Nevertheless, this is only speculation and

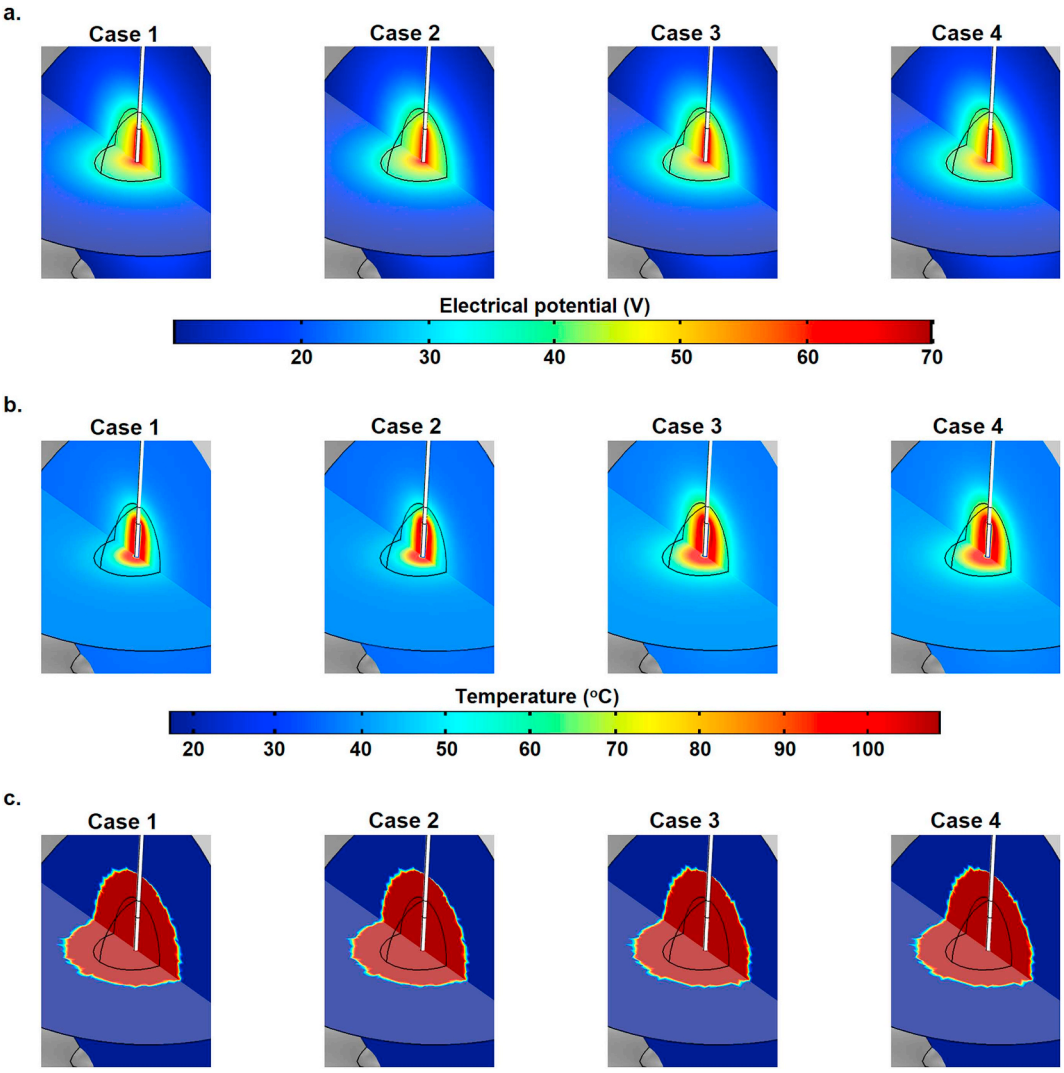

Fig. 8. Contours of the a) electrical potential distribution at the start of ablation, b) temperature distribution at the point before the first roll-off and c) thermal damage distribution after 10 min of ablation, obtained using Model C for Cases 1 to 4.

Table 4
Thermal damage volume obtained for Cases 1 to 4 of Model C (tumour far from the liver boundary).

	Thermal damage volume (cm)3
Case 1	33.556
Case 2	33.225
Case 3	34.280
Case 4	34.293

more investigation into the matter is needed for further clarification.

There are several limitations to the present study that can be further improved on in future studies. Firstly, the tumour domain, which is built based on an ellipsoid, is hypothetical. In reality, tumours are irregularly-shaped. Although some of the patient data from the publicly-available database contains the tumour, they have not been considered during the segmentation process. This is to simplify the modelling process as well as the prescription of boundary conditions in the present study. Although the use of a more realistic tumour domain would lend further credence to the results of the present study, the construction of the tumour based on an ellipsoid is not expected to affect the conclusion deduced. Secondly, tumours that are located very near to the boundary may lead to the ablation zone to be adjacent to organs such as the gastrointestinal tract, the diaphragm and the bile duct. The uncertainty associated with the modelling of the electrical and thermal effects due to the proximity of these structures have led to the occlusion from the RFA models in the present study. Nevertheless, their effects cannot be ignored and they should be the subject of further investigations in the future. Thirdly, the present study has not included the effects of nearby blood vessels that are in abundance inside the liver. While the thermal effects due to blood flow inside the micro capillaries can be accurately simulated using the Pennes bioheat equation, large blood vessels, such as the portal vein and the hepatic artery may have to be modelled explicitly. This is especially true if the tumour is in the vicinity of these structures. The blood vessel was not considered in the present study due to the difficulty in incorporating an hypothetical vessel into the liver model. Furthermore, it is to the authors' opinion that the inclusion of the blood vessel at this stage may obscure the effects due to the different boundary conditions, which deviates from the objective and the scope of the present study.

5. Conclusions

The present study was set out to investigate the effects of different electrical and thermal boundary conditions prescribed across the exterior boundaries of the model domains on the prediction outcome of RFA simulations. Ground and the Robin type boundary condition that mimics the natural flow of electrical current to an infinite space were

considered for the electrical field, while body temperature and thermal insulation conditions were considered for the thermal field. The results show that these different boundary conditions affected the prediction outcomes of RFA simulations in terms of the heating profile, the electrical potential distribution, the temperature distribution and the thermal damage volume. The use of the ground or the body temperature condition resulted in the prediction of smaller thermal coagulation volume than the case when the Robin type condition or the thermal insulation condition is prescribed. It is not possible at this stage to conclude if the ground and body temperature condition is less accurate than the electrical and thermal insulation conditions or vice versa. However, experimental and clinical observations reported from the literature appear to suggest that the predictions produced using the Robin type and the thermal insulation boundary conditions are more realistic. While the present study could not firmly identify the correct electrical and thermal boundary conditions to be prescribed, the results suggest that there is cause for concern when it comes to the selection of the proper electrical and thermal boundary conditions to be prescribed across the exterior surfaces of RFA models in the case where the tumour is located at the peripheral region of the liver.

Conflicts of interest

None declared.

Acknowledgments

The authors are grateful to the Ministry of Energy, Science, Technology, Environment and Climate Change (formerly Ministry of Science, Technology and Innovation), Malaysia for funding this work through the ScienceFund grant scheme under the project 06-02-10-SF0317. EHO and JJF would like to thank Monash University Malaysia (MUM) for supporting the high speed computing system for the current research investigation (Research Project No: 5140810-113-00).

Appendix A. Supplementary data

Supplementary data to this article can be found online at https://doi.org/10.1016/j.compbiomed.2019.01.003.

References

[1] S. Singh, R. Repaka, Temperature-controlled radiofrequency ablation of different tissues using two-compartment models, Int. J. Hyperther. 33 (2016) 122–134.
[2] M. Trujillo, J. Bon, M.J. Rivera, F. Burdío, E. Berjano, Computer modelling of an impedance-controlled pulsing protocol for rf tumour ablation with a cooled electrode, Int. J. Hyperther. 32 (2016) 931–939.
[3] M. Trujillo, J. Bon, E. Berjano, Computational modelling of internally cooled wet (ICW) electrodes for radiofrequency ablation: impact of rehydration, thermla convection and electrical conductivity, Int. J. Hyperther. 44 (2017) 624–634.
[4] I. Altrogge, T. Preusser, T. Kröger, C. Büskens, P.L. Pereira, D. Schmidt, H.-O. Peitgen, Multiscale optimization of the probe placement for radiofrequency ablation, Acad. Radiol. 14 (2007) 1310–1324.
[5] T. Kröger, S. Pannier, M. Kaliske, I. Altrögge, W. Graf, T. Preusser, Optimal applicator placement in hepatic radiofrequency ablation on the basis of rare data, Comput. Methods Biomech. Biomed. Eng. 13 (2010) 431–440.
[6] A.M. Qadri, N.J.Y. Chia, E.H. Ooi, Effects of saline volume on lesion formation during saline-infused radiofrequency ablation, Appl. Math. Model. 43 (2017) 360–371.
[7] E.H. Ooi, N.J.Y. Chia, E.T. Ooi, J.J. Foo, I.Y. Liao, S.R. Nair, A.F.M. Ali, Comparison between single- and dual-porosity models for fluid transport in predicting lesion volume following saline-insued radiofrequency ablation, Int. J. Hyperther. 34 (2018) 1142–1156.
[8] M.L. Neal, R. Kerckhoffs, Current progress in patient-specific modeling, Briefings Bioinf. 11 (2010) 111–126.
[9] G. Zorbas, T. Samaras, Simulation of radiofrequency ablation in real human anatomy, Int. J. Hyperther. 30 (2014) 570–578.
[10] C. Rieder, T. Kroger, C. Schumann, H. Hahn, GPU based real time approximation of the ablation zone for radiofrequency ablation, IEEE Trans. Visual. Comput. Graph. 17 (2011) 1812–1821.
[11] C. Audigier, T. Mansi, H. Delingette, S. Rapaka, V. Mihalef, P. Sharma, A. Kamen, D. Carnegie, E. Boctor, M. Choti, Lattice Boltzmann Method for fast patient-specific simulation of liver tumor ablation from CT images, in: K. Mori, I. Sakuma, Y. Sato, C. Barillot, N. Navab (Eds.), MICCAI - Medical Image Computing and Computer Assisted Intervention, Vol. 8151 of Lecture Notes in Computer Science, 2013, pp. 323–330.
[12] C. Audigier, T. Mansi, H. Delingette, S. Rapaka, V. Mihalef, D. Carnegie, E. Boctor, M. Choti, A. Kamen, N. Ayache, D. Comaniciu, Efficient Lattice Boltzmann solver for patient-specific radiofrequency ablation of hepatic tumors, IEEE Trans. Med. Imag. 34 (2015) 1576–1589.
[13] S.J. Payne, R. Flanagan, M. Pollari, T. Alhonnoro, C. Bost, D. O'Neill, T. Peng, P. Stiegler, Image-based multi-scale modelling and validation of radio-frequency ablation in liver tumours, Philosoph. Transact. Roy. Soc. A 369 (2011) 4233–4254.
[14] P. Voglreiter, P. Mariappan, M. Pollari, R. Flanagan, R.B. Sequeiros, R.H. Portugaller, J. Fütterer, D. Schmalstieg, M. Kolesnik, M. Moche, R.F.A. Guardian, Comprehensive simulation of radiofrequency ablation treatment of liver tumors, Sci. Rep. 8 (2018) 787.
[15] 3d-ircadb 01. URL https://www.ircad.fr/research/3d-ircadb-01/.
[16] D.-J. Kroon, Smooth triangulated mesh. URL https://www.mathworks.com/matlabcentral/fileexchange/26710-smooth-triangulated-mesh.
[17] S.K. Hall, E.H. Ooi, S.J. Payne, A mathematical framework for minimally invasive tumor ablation therapies, Crit. Rev. Biomed. Eng. 42 (2014) 383–417.
[18] H.H. Pennes, Analysis of tissue and arterial blood temperatures in the resting human forearm, J. Appl. Physiol. 1 (1948) 93–122.
[19] J.A. Pearce, Models for thermal damage in tissues: processes and applications, Crit. Rev. Biomed. Eng. 38 (2010) 1–20.
[20] F. Burdío, E.J. Berjano, A. Navarro, J.M. Burdio, L. Grande, A. Gonzalez, I. Cruz, A. Guemes, R. Sousa, J. Subira, T. Castiella, I. Poves, J. Lequerica, Research and development of a new RF-assisted device for blood rapid transection of the liver: computational modeling and in vivo experiments, Biomed. Eng. Online 8 (2009) 6.
[21] C.L. Antunes, T.R. Almeida, N. Raposeiro, Saline-enhanced RF ablatio on a cholangiocarcinoma: a numerical simulation, Int. J. Computat. Math. Electric. Electron. Eng. 31 (2012) 1055–1066.
[22] M. Trujillo, E. Berjano, Review of the mathematical functions used to model the temperature dependence of electrical and thermal conductivities of biological tissue in radiofrequency ablation, Int. J. Hyperther. 29 (2013) 590–597.
[23] S.K. Hall, E.H. Ooi, S.J. Payne, Cell death, perfusion and electrical parameters are critical in models of hepatic radiofrequency ablation, Int. J. Hyperther. 31 (2015) 538–550.
[24] S.N. Goldberg, M.C. Stein, G.S. Gazelle, R.G. Sheiman, J.B. Kruskal, M.E. Clouse, Percutaneous radiofrequency tissue ablation: optimization of pulsed-radio-frequency technique to increase coagulation necrosis, J. Vasc. Intervent. Radiol. 10 (1999) 907–916.
[25] M. Trujillo, J. Alba, E. Berjano, Relationship between roll-off occurrence and spatial distribution of dehydrated tissue during RF ablation with cooled electrodes, Int. J. Hyperther. 28 (2012) 62–68.
[26] T. Livarghi, L. Solbiati, M.F. Meloni, G.S. Gazelle, E.F. Halpern, S.N. Goldberg, Treatment of focal liver tumors with percutaneous radio-frequency ablation: complications encountered in a multicenter study, Radiology 226 (2003) 441–451.
[27] M.J. Howenstein, K.T. Sato, Complications of radiofrequency ablation of hepatic, pulmonary and renal neoplasms, Semin. Intervent. Radiol. 27 (2010) 285–295.
[28] H. Choi, E. M. Loyer, R. A. DuBrow, H. Kaur, C. L. David, S. Huang, S. Curley, C. Charnsangavej, Radio-frequency ablation of liver tumors: assessment of therapeutic response and complications, Radiographics 21.
[29] M.F. Meloni, S.N. Goldberg, V. Moser, G. Piazza, T. Livarghi, Colonic perforation and abscess following radiofrequency ablation treatment of hepatoma, Eur. J. Ultrasound 15 (2002) 73–76.
[30] J.M. Lee, J.K. Han, J.M. Chang, S.Y. Chung, S.H. Kim, M.W. Lee, B.I. Choi, Radiofrequency ablation of the porcine liver in vivo: increased coagulation with an internally cooled perfusion electrode, Acad. Radiol. 13 (2006) 343–352.
[31] D.H. Haemmerich, Finite Element Modeling of Hepatic Radiofrequency Ablation, Ph.D. thesis University of Wisconsin-Madison, 2001.
[32] U. Zurbuchen, F. Poch, O. Gemeinhardt, M.E. Kreis, S.M. Niehues, J.L. Vahldieck, K.S. Lehmann, Determination of the electrical conductivity of human liver metastases: impact on therapy planning in the radiofrequency ablation of liver tumors, Acta Radiol. 58 (2017) 164–169.
[33] K.R. Holmes, M.M. Chen, Local thermal conductivity of Para-7 fibrosarcoma in hamster, Advances in Bioengineering, ASME, New York, 1979, pp. 147–149.
[34] J. Mattson, M. Alpsten, L. Appelgren, H.I. Peterson, Influence of Noradrenalin on local tumor blood flow, Eur. J. Cancer 16 (1980) 99–102.
[35] S. Jacques, S. Rastegar, S. Thomsen, M. Motamedi, The role of dynamic changes in blood perfusion and optical properties in laser coagulation tissue, IEEE J. Sel. Top. Quant. Electron. 2 (1996) 922–933.
[36] D. Haemmerich, B.J. Wood, Hepatic radiofrequency ablation at low frequencies preferentially heats tumour tissue, Int. J. Hyperther. 22 (2006) 563–574.